

# Constrained C<sub>2</sub> adsorbate orientation enables CO-to-acetate electroreduction

<https://doi.org/10.1038/s41586-023-05918-8>

Received: 25 January 2022

Accepted: 2 March 2023

Published online: 3 May 2023

 Check for updates

Jian Jin<sup>1,2,18</sup>, Joshua Wicks<sup>3,18</sup>, QiuHong Min<sup>1,18</sup>, Jun Li<sup>4,18</sup>, Yongfeng Hu<sup>5</sup>, Jingyuan Ma<sup>6,7</sup>, Yu Wang<sup>6,7</sup>, Zheng Jiang<sup>6,7</sup>, Yi Xu<sup>8</sup>, Ruihu Lu<sup>19</sup>, Gangzheng Si<sup>1</sup>, Panagiotis Papangelakis<sup>8</sup>, Mohsen Shakouri<sup>10</sup>, Qunfeng Xiao<sup>10</sup>, Pengfei Ou<sup>3</sup>, Xue Wang<sup>3</sup>, Zhu Chen<sup>3</sup>, Wei Zhang<sup>11</sup>, Kesong Yu<sup>11</sup>, Jiayang Song<sup>1</sup>, Xiaohang Jiang<sup>1</sup>, Peng Qiu<sup>1</sup>, Yuanhao Lou<sup>1</sup>, Dan Wu<sup>1</sup>, Yu Mao<sup>9</sup>, Adnan Ozden<sup>8</sup>, Chundong Wang<sup>1</sup>, Bao Yu Xia<sup>12</sup>, Xiaobing Hu<sup>13,14</sup>, Vinayak P. Dravid<sup>13,14</sup>, Yun-Mui Yiu<sup>15</sup>, Tsun-Kong Sham<sup>15</sup>, Ziyun Wang<sup>9</sup>, David Sinton<sup>8</sup>, Liqiang Mai<sup>11</sup>, Edward H. Sargent<sup>3,16,17</sup> & Yuanjie Pang<sup>1</sup>

The carbon dioxide and carbon monoxide electroreduction reactions, when powered using low-carbon electricity, offer pathways to the decarbonization of chemical manufacture<sup>1,2</sup>. Copper (Cu) is relied on today for carbon–carbon coupling, in which it produces mixtures of more than ten C<sub>2+</sub> chemicals<sup>3–6</sup>: a long-standing challenge lies in achieving selectivity to a single principal C<sub>2+</sub> product<sup>7–9</sup>. Acetate is one such C<sub>2</sub> compound on the path to the large but fossil-derived acetic acid market. Here we pursued dispersing a low concentration of Cu atoms in a host metal to favour the stabilization of ketenes<sup>10</sup>—chemical intermediates that are bound in monodentate fashion to the electrocatalyst. We synthesize Cu-in-Ag dilute (about 1 atomic per cent of Cu) alloy materials that we find to be highly selective for acetate electrosynthesis from CO at high \*CO coverage, implemented at 10 atm pressure. Operando X-ray absorption spectroscopy indicates *in situ*-generated Cu clusters consisting of <4 atoms as active sites. We report a 12:1 ratio, an order of magnitude increase compared to the best previous reports, in the selectivity for acetate relative to all other products observed from the carbon monoxide electroreduction reaction. Combining catalyst design and reactor engineering, we achieve a CO-to-acetate Faradaic efficiency of 91% and report a Faradaic efficiency of 85% with an 820-h operating time. High selectivity benefits energy efficiency and downstream separation across all carbon-based electrochemical transformations, highlighting the importance of maximizing the Faradaic efficiency towards a single C<sub>2+</sub> product<sup>11</sup>.

Acetic acid has annual production volumes of more than 18 million tonnes and a market value approaching US\$10 billion per year<sup>12</sup>. It is an industrial solvent for terephthalic acid production and a precursor to vinyl acetate for paints, adhesives and coatings<sup>13</sup>. Sodium and potassium acetates, which are derived from acetic acid<sup>14</sup>, are useful as food additives. Industrial production of acetic acid and acetate requires a multi-step process: thermocatalytic conversion of syngas to methanol at 5–10 MPa and 250 °C (ref. 15), followed by methyl carbonylation<sup>16</sup> of methanol and CO to form acetic acid. This process, derived from fossil fuels, generates 1.6 kg of cradle-to-gate CO<sub>2</sub>-equivalent emissions per kilogram of acetic acid produced<sup>17</sup>.

Electrochemical systems powered by renewable electricity have achieved the synthesis of acetate and acetic acid using CO<sub>2</sub> or CO, and water, as reagents<sup>18,19</sup>. Acetate to acetic acid conversion is readily achievable by the *in situ* neutralization of acetate<sup>20</sup>. Direct aqueous CO<sub>2</sub>-to-acetate electroreduction has shown impressive selectivity reaching a Faradaic efficiency (FE) of 49% (ref. 21); however, the full-cell potential was 6.6 V, compared to the theoretical energy value of the acetate–O<sub>2</sub> couple of 0.91 V, resulting in an overall energy consumption of 285 GJ per tonne of potassium acetate produced. To improve both voltage and acetate selectivity, tandem carbon dioxide electroreduction

<sup>1</sup>School of Optical and Electronic Information, Wuhan National Laboratory for Optoelectronics, Huazhong University of Science and Technology, Wuhan, China. <sup>2</sup>School of Environmental Science and Engineering, Huazhong University of Science and Technology, Wuhan, China. <sup>3</sup>Department of Electrical and Computer Engineering, University of Toronto, Toronto, Ontario, Canada. <sup>4</sup>Frontiers Science Center for Transformative Molecules, Shanghai Jiao Tong University, Shanghai, China. <sup>5</sup>Department of Chemical & Biological Engineering, University of Saskatchewan, Saskatoon, Saskatchewan, Canada. <sup>6</sup>Shanghai Synchrotron Radiation Facility, Zhangjiang National Lab, Shanghai Advanced Research Institute, Chinese Academy of Sciences, Shanghai, China. <sup>7</sup>Shanghai Institute of Applied Physics, Chinese Academy of Sciences, Shanghai, China. <sup>8</sup>Department of Mechanical and Industrial Engineering, University of Toronto, Toronto, Ontario, Canada. <sup>9</sup>School of Chemical Sciences, The University of Auckland, Auckland, New Zealand. <sup>10</sup>Canadian Light Source, Inc., University of Saskatchewan, Saskatoon, Saskatchewan, Canada. <sup>11</sup>State Key Laboratory of Advanced Technology for Materials Synthesis and Processing, School of Materials Science and Engineering, Wuhan University of Technology, Wuhan, China. <sup>12</sup>Key Laboratory of Material Chemistry for Energy Conversion and Storage (Ministry of Education), School of Chemistry and Chemical Engineering, Huazhong University of Science and Technology, Wuhan, China. <sup>13</sup>Department of Materials Science and Engineering, Northwestern University, Evanston, IL, USA. <sup>14</sup>The NUANCE Center, Northwestern University, Evanston, IL, USA. <sup>15</sup>Department of Chemistry, Western University, London, ON, Canada. <sup>16</sup>Department of Chemistry, Northwestern University, Evanston, IL, USA. <sup>17</sup>Department of Electrical and Computer Engineering, Northwestern University, Evanston, IL, USA. <sup>18</sup>These authors contributed equally: Jian Jin, Joshua Wicks, QiuHong Min, Jun Li.  e-mail: mlq518@whut.edu.cn; ted.sargent@utoronto.ca; yuanjie\_pang@hust.edu.cn

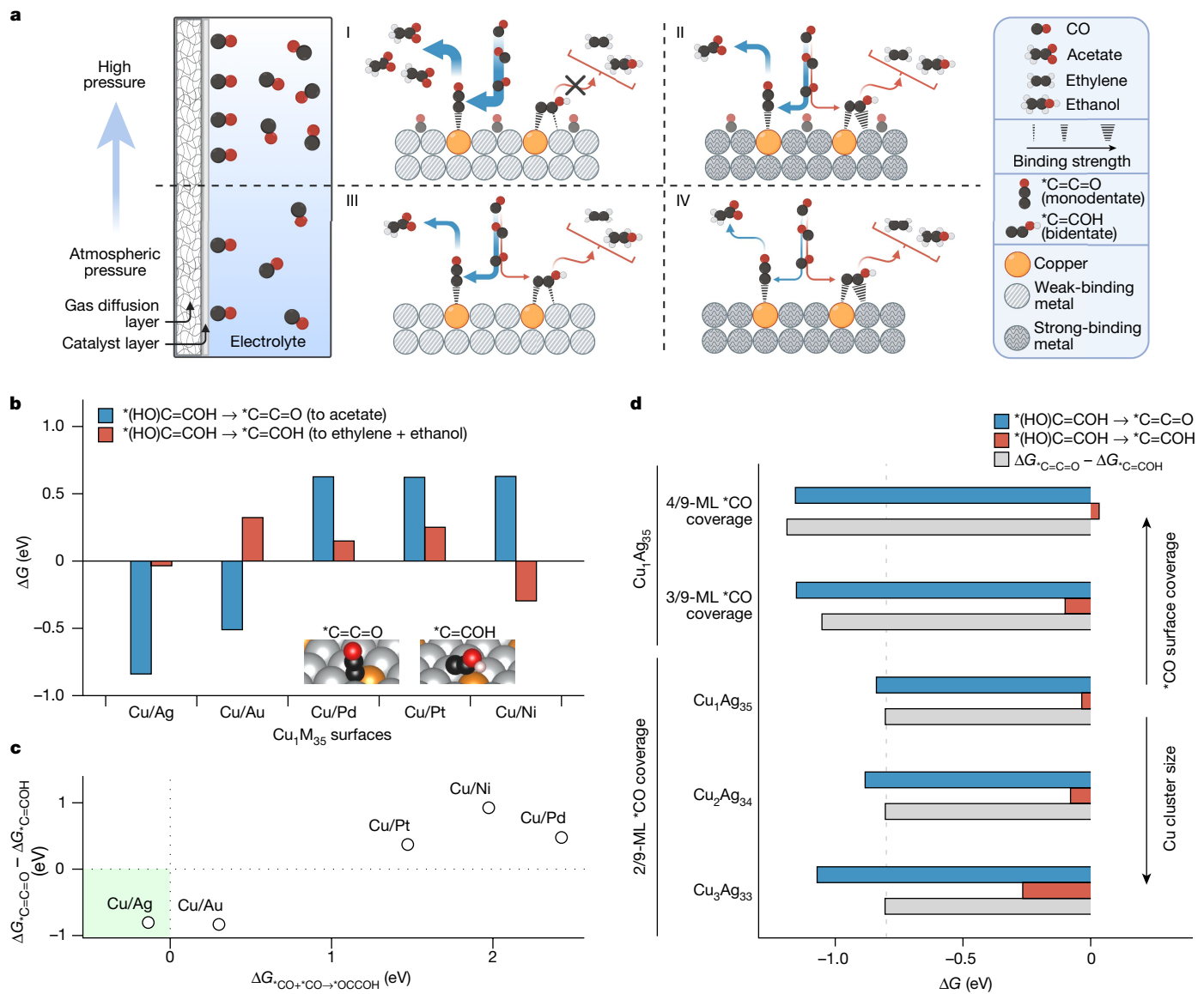


**Fig. 1 | CO-to-acetate electrocatalyst design.** **a**, Schematic illustration of design matrix considering both CO pressure and host metal for Cu/M-DA materials. Quadrant I: increased \*CO coverage due to pressure and weak-binding host metal lead to extreme selectivity towards acetate (acetate/(other  $C_2$ ) ratio > 5). Quadrant II (strong binding host metal and high pressure) and quadrant III (weak-binding host metal and atmospheric pressure): improved selectivity to acetate (2 < acetate/(other  $C_2$ ) ratio < 5). Quadrant IV: strong binding host metal at atmospheric pressure leads to a mixed  $C_2$  product distribution (acetate/(other  $C_2$ ) ratio < 2). **b**, Comparison of the bifurcation of

$^{*(OH)C=COH \rightarrow *C=C=O}$  and  $^{*(OH)C=COH \rightarrow *C=COH}$  reaction pathways as an indicator for acetate selectivity across a series of Cu/M-DAs (modelled as  $Cu_M_{35}$ , M = Ag, Au, Pd, Pt or Ni) surfaces at 0 V. **c**, Combination of \*CO + \*CO coupling energy and the difference between branching acetate and ethylene + ethanol reaction pathways highlights the down-selection of Cu/Ag-DA materials from the initial candidate list. **d**, Branching of acetate and ethylene + ethanol reaction pathways with explicitly modelled \*CO coverage and Cu cluster size. ML, monolayer. **a** was created with BioRender.com.

reaction (CO<sub>2</sub>RR) has shown promise: by pairing CO<sub>2</sub>-to-CO solid oxide electrolyser cell (SOEC) technology, which provides FE greater than 95% (refs. 22,23), with a CO-to-C<sub>2+</sub> electrolyser<sup>2</sup>, tandem CO<sub>2</sub>RR benefits from a more energy- and carbon-efficient CO<sub>2</sub>-to-CO step. Starting from CO reduces complexity because two fewer electrons per CO molecule are needed to obtain the same product as from CO<sub>2</sub> (refs. 24,25). Current state-of-the-art CO-to-acetate electroconversion has a comparable FE to that in the direct CO<sub>2</sub>RR approach but was achieved at a much lower full-cell potential of about 4 V, showing promise with a lower overall energy consumption of 231 GJ per tonne of potassium acetate<sup>20</sup>. For economic viability, we aim to achieve a comparably high FE (>90%)<sup>11</sup> between SOEC and CO-to-acetate reactors.

Carbon–carbon (C–C) coupling electrochemistry relies on Cu-based catalysts<sup>26</sup>; these, however, have low selectivity among the many

possible C<sub>2</sub> products. We noted that C<sub>2</sub> intermediates have diverse binding orientations, and indeed certain intermediates, such as those bidentate-bound to Cu (binding of the intermediate at two points of contact), favour ethylene, ethanol and 1-propanol<sup>15,20</sup>.

By contrast, monodentate C<sub>2</sub> intermediates have a one-to-one mapping to acetate<sup>10</sup>. This motivated us to pursue small, isolated, Cu domains in the catalyst surface, hoping to promote acetate relative to the products that arise from bidentate-bound intermediates. To address the lowered rate of C–C coupling when the catalyst surface is a sea of non-Cu atoms, we would exploit the use of modest pressures of CO. In this way (Fig. 1a), we would combine monodentate-favouring isolated Cu clusters with increased \*CO coverage to seek increased acetate selectivity in carbon monoxide electroreduction reaction (CORR).

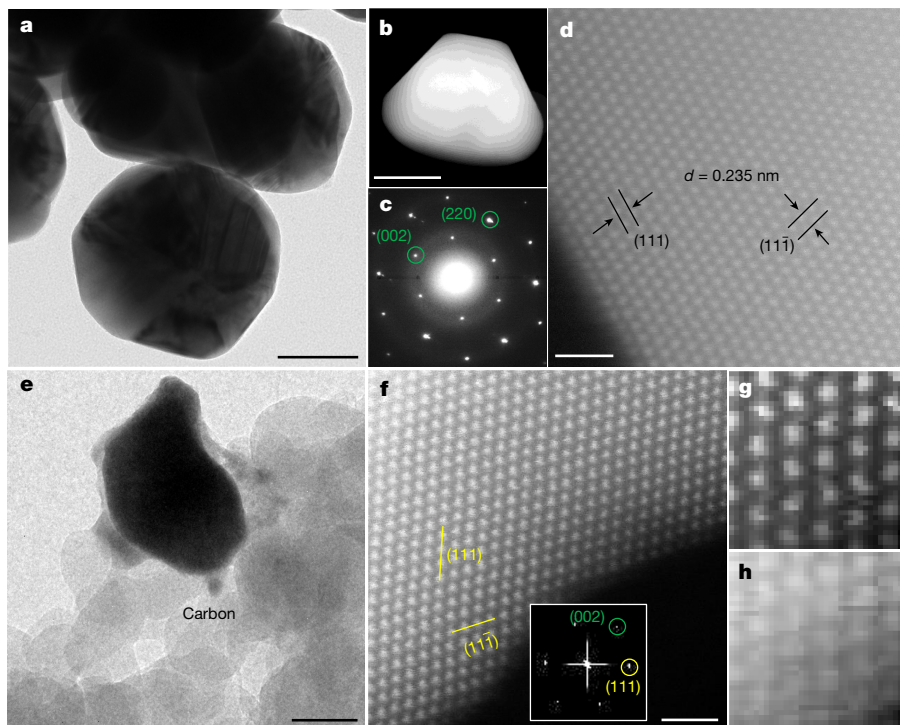


**Fig. 2 | Structural characterization of Cu/Ag-DA nanoparticles.** **a,b**, TEM (a) and HAADF scanning TEM (b) images of the as-synthesized catalyst before CORR. Scale bars, 100 nm (a) and 50 nm (b). **c**, Electron diffraction patterns of the nanoparticles shown in b. **d**, Atomic-resolution HAADF image of nanoparticles

before CORR. Scale bar, 1 nm. **e,f**, TEM (e) and atomic-resolution HAADF (f) images of catalysts after CORR. Inset in f is the digital fast Fourier transform image. Scale bars, 50 nm (e) and 1 nm (f). **g,h**, ADF image (g) and map (h) of Ag signal within 390–490 eV based on reconstructed data cube.

Using density functional theory, we first examine the branching of  $^{*}(\text{OH})\text{C}=\text{COH} \rightarrow ^{*}\text{C}=\text{C}=\text{O}$  (monodentate; one-to-one mapping to acetate) versus  $^{*}(\text{OH})\text{C}=\text{COH} \rightarrow ^{*}\text{C}=\text{COH}$  (bidentate; one-to-many mapping to ethylene, ethanol and *n*-propanol)<sup>10</sup> to explore acetate selectivity across a series of (111) Cu-in-M dilute alloy (Cu/M-DA; modelled as  $\text{Cu}_1\text{M}_{35}$ , M = Ag, Au, Pd, Pt, Ni) surfaces in Fig. 1b<sup>10</sup>. These metals were selected because they have the same bulk crystallographic space group as Cu ( $Fm\bar{3}m$ ) and include metals with traditionally weak (Ag, Au) and strong (Pd, Pt, Ni) CO binding energies. A single Cu atom in this model represents an atomic concentration of about 3% expected for a dilute alloy. We used the computational hydrogen electrode model and a potential of 0 V to compute the reaction energies (data for other applied potentials are in Supplementary Figs. 1 and 2). The use of Ag and Au as Cu hosts favours monodentate-binding  $^{*}\text{C}=\text{C}=\text{O}$  over bidentate-binding  $^{*}\text{C}=\text{COH}$ , consistent with the picture that surrounding a Cu atom with a metal having weaker adsorption for carbon-based adsorbates stabilizes monodentate  $\text{C}_2$  adsorbates. For these adsorbates to exist on the largely non-Cu surfaces, the coupling of two  $^{*}\text{CO}$  adsorbates on that same surface should also be feasible<sup>9,27</sup>. In Fig. 1c, we model  $^{*}\text{CO}-^{*}\text{CO}$  coupling to  $^{*}\text{OCCO}$  and the subsequent proton transfer from water to  $^{*}\text{OCCOH}$  along the *x* axis. The  $\text{Cu}_1\text{Ag}_{35}$  surface is shown to favour  $^{*}\text{CO}$  dimerization over  $\text{Cu}_1\text{Au}_{35}$ , and the unfavourable coupling on  $\text{Cu}_1\text{Pd}_{35}$ ,  $\text{Cu}_1\text{Pt}_{35}$  and  $\text{Cu}_1\text{Ni}_{35}$  is attributed to the strong adsorption of  $^{*}\text{CO}$ . This result, although promising, would require that sufficient surface coverage of  $^{*}\text{CO}$  be obtained to support a sufficient rate of  $^{*}\text{CO}$  dimerization. A coverage-dependent phase diagram<sup>28</sup> (Supplementary Fig. 3) shows that increasing the partial pressure of CO is key to enabling use of the Cu-in-Ag dilute alloy (Cu/Ag-DA) catalyst materials. Adding  $^{*}\text{CO}$  species to the surface (Fig. 1d) increases the extent to which the overall acetate/(all other  $\text{C}_{2+}$  pathways) ratio is favoured by a further 0.36 eV. We also note that perfect single atoms are not mandatory: clusters of two and three Cu atoms ( $\text{Cu}_2\text{Ag}_{34}$  and  $\text{Cu}_3\text{Ag}_{33}$ ) also favour the  $^{*}\text{C}=\text{C}=\text{O}$  adsorbate over  $^{*}\text{C}=\text{COH}$  to a similar extent as the  $\text{Cu}_1\text{Ag}_{35}$  model (Fig. 1d).

We pursued the synthesis of Cu/M-DA catalysts in which M = Ag, Au or Ni, down-selecting from our original list to include the most promising host material (Ag), a positive control (Au) and a negative control (Ni). We used a one-pot synthesis for alloy nanoparticles with two precursors<sup>29</sup>, one for Cu, the other for the host metal M, and we raise the nucleation energy of Cu above that of the host metal using chloride anions<sup>30</sup>. In this way, we control the growth rates and crystalline phases of both metals, seeking catalysts with Cu atoms evenly dispersed in the host. Focusing on Cu/Ag-DA, scanning electron microscopy (SEM; Supplementary Fig. 4) shows Cu/Ag-DA nanoparticles with an average diameter of 140 nm and a bulk Cu/Ag atomic ratio of about 1% (inductively coupled plasma optical emission spectroscopy and X-ray photoelectron spectroscopy; Supplementary Fig. 5 and Supplementary Table 1). The morphology (Fig. 2a,b and Supplementary Figs. 4 and 6) and electrochemical surface area (Supplementary Fig. 7) of the as-synthesized nanoparticles match the post-CORR samples after 1 h of operation. SEM with energy-dispersive X-ray spectroscopy (SEM-EDS; Supplementary Figs. 8 and 9) and transmission electron microscopy with EDS (TEM-EDS; Supplementary Figs. 10 and 11) return both Cu and Ag signals within a single particle. Electron diffraction, high-resolution TEM, fast Fourier transform thereof (Fig. 2c and Supplementary Fig. 10d,e,i,j) and X-ray diffraction (Supplementary Fig. 12) indicate an Ag lattice without crystalline Cu features, both before and after CORR. TEM and high-angle annular dark-field (HAADF) scanning TEM images of the Cu/Ag-DA, before and after CORR (Fig. 2d,e-h), detect no evident segregation of Cu, indicating a uniform distribution of Cu atoms within the Ag lattice. We carried out analogous materials characterization for Cu/Au-DA and Cu/Ni-DA and obtained comparable results (Supplementary Figs. 13–15 and Supplementary Table 2).

We then carried out X-ray absorption spectroscopy (XAS) to examine the electronic structure during CORR. Ex situ X-ray absorption near-edge structure (XANES) results (Fig. 3a) show that Cu in the Cu/Ag-DA catalyst is oxidized before and after CORR, and no Cu–Cu

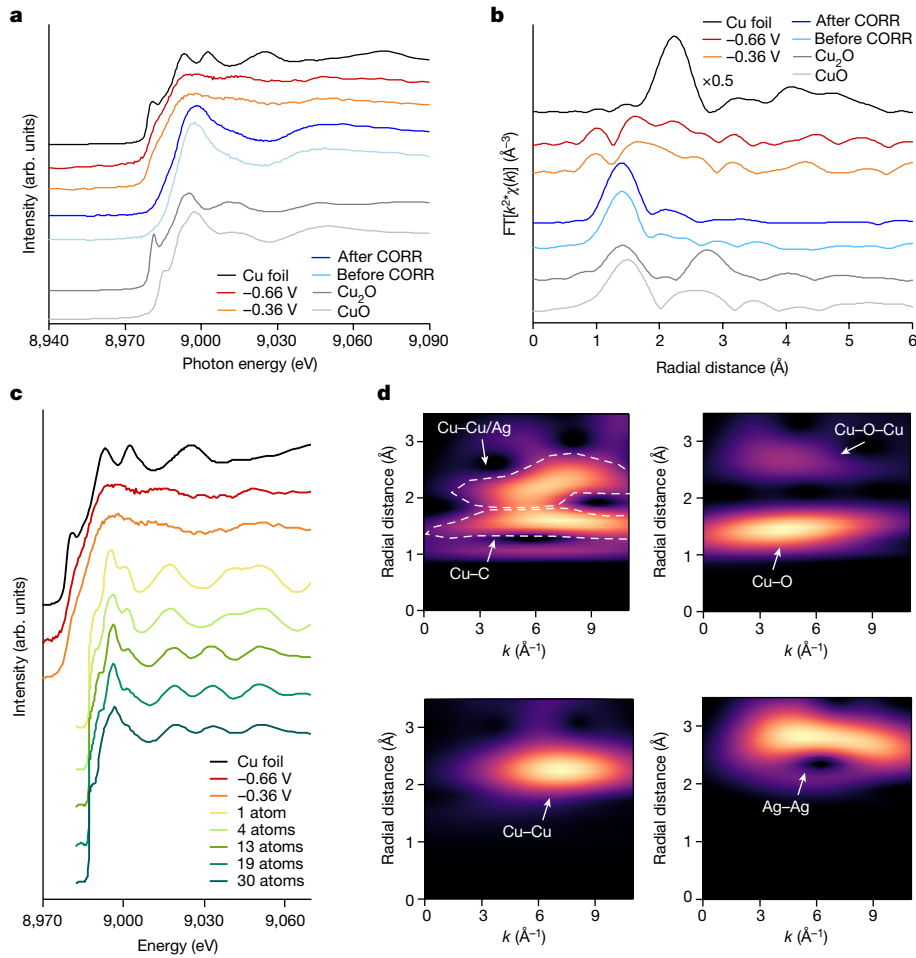


**Fig. 3 | XAS analysis.** **a,b**, Normalized Cu K-edge XANES (**a**) and Fourier transform of the EXAFS spectra (**b**) of the Cu/Ag-DA catalysts (before, during and after CORR), with Cu foil,  $\text{Cu}_2\text{O}$  and  $\text{CuO}$  as references. FT, Fourier transform. **c**, Cu K-edge XAS spectra of Cu foil, and Cu/Ag-DA catalysts at

-0.36 V and -0.66 V versus RHE, and calculated XAS spectra of Cu/Ag clusters containing 1–30 Cu atoms in a 55-atom slab. **d**, Wavelet transform plots of the Cu/Ag-DA catalyst at -0.66 V versus RHE during CORR (top left),  $\text{Cu}_2\text{O}$  (top right), Cu foil (bottom left) and Ag foil (bottom right).

bond formation is observed in the catalyst from the corresponding extended X-ray absorption fine structure (EXAFS; Fig. 3b), suggesting an atomic dispersion of Cu in the metallic Ag lattice (Supplementary Fig. 16). Operando XAS characterization in a flow cell reactor with an X-ray-transparent window<sup>31</sup> (Supplementary Fig. 17) enabled us to evaluate the catalyst structure under realistic reaction conditions. During CORR at -0.36 V and -0.66 V versus the reversible hydrogen electrode (RHE), the Cu K-edge white-line intensities decrease (Fig. 3a), and the corresponding EXAFS spectra indicate low-coordination clusters of Cu atoms in Ag under both reduction potentials.

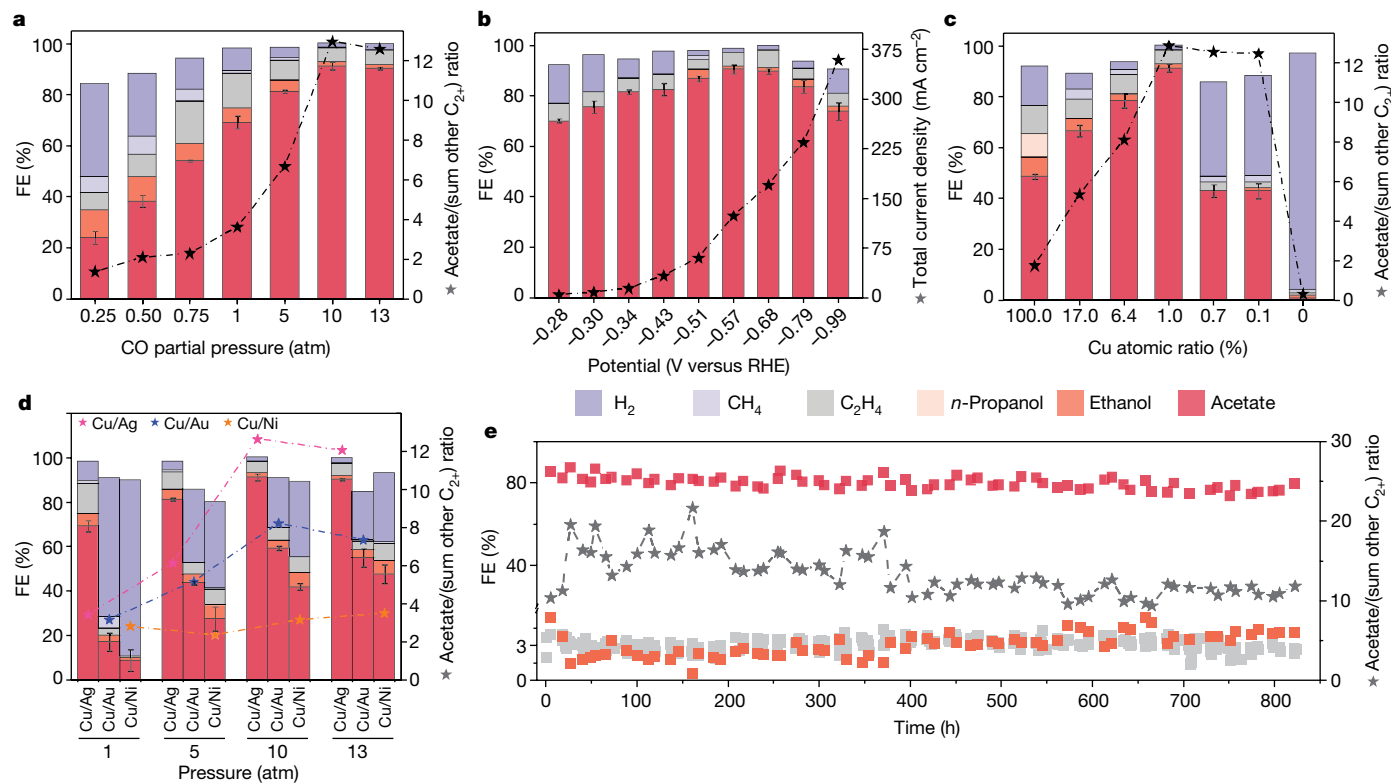
To assess the size of these isolated Cu clusters, we computed Cu K-edge XANES spectra of Cu-in-Ag clusters containing 1 to 30 Cu atoms (Fig. 3c). By comparing experimental and theoretically computed spectra, we found that clusters with 1–4 Cu atoms show a similar spectral pattern to that of the Cu/Ag-DA catalysts during CORR. In addition, we carried out time-dependent operando XAS measurements (Supplementary Fig. 18) and showed that Cu clusters in Ag retain their structure over time at 0.36 V and -0.66 V versus RHE. Taken together, these findings suggest that Cu/Ag-DA contains Cu clusters of an average size of about four or fewer atoms.

Figure 3d shows a maximum wavelet transform of Cu/Ag-DA between 4 and 8  $\text{\AA}^{-1}$  at a radial distance range of 2–3  $\text{\AA}$ , which corresponds to Cu–Cu and Cu–Ag bonding. These results are distinct compared to the wavelet transform plots of Cu foil (6–8  $\text{\AA}^{-1}$  and 2–2.5  $\text{\AA}$ ) and Ag foil (4–8  $\text{\AA}^{-1}$  and 2.5–3  $\text{\AA}$ ), suggesting a strong interaction of Cu with Ag

in Cu/Ag-DA. Notably, an additional band appears on Cu/Ag-DA at a maximum wavelet transform of 5–9  $\text{\AA}^{-1}$  and a radial distance of about 1.6  $\text{\AA}$  that is distinct from the Cu–O bonding (3–7  $\text{\AA}^{-1}$  at about 1.4  $\text{\AA}$ ) in  $\text{Cu}_2\text{O}$ , and that we attribute to Cu–C interaction during CORR. We fitted the EXAFS spectra (Supplementary Fig. 19 and Supplementary Table 3) of Cu/Ag-DA during CORR and found that a Cu–C bond length of about 2.0  $\text{\AA}$  is consistent with metal–C bond lengths reported previously<sup>32</sup>. As the applied potential changes from -0.36 V to -0.66 V, the average Cu–Cu coordination number increases from 0.4 to 0.6 whereas both Cu–C and Cu–Ag coordination numbers decrease. This suggests that, at more negative potentials, the average Cu cluster size increases slightly to the order of 4 atoms, and the average interaction between Cu and adsorbed C species weakens.

In situ Raman spectroscopy during CORR (Supplementary Fig. 20) shows several peaks corresponding to  $^{*}\text{CO}$  adsorption on Cu and Ag sites and a major peak at about 541  $\text{cm}^{-1}$ . When CO is substituted for an inert gas such as  $\text{N}_2$ , this peak is not observed. The wavenumber of the peak decreases when using  $^{13}\text{CO}$  gas. These observations suggest assignment to a carbon-based reaction intermediate. Vibrational frequency calculations (Supplementary Tables 4 and 5) on the model  $\text{Cu}_1\text{Ag}_{35}$  slab find that this major peak is most closely associated with  $^{*}\text{C}=\text{C}=\text{O}$  or  $^{*}(\text{OH})\text{C}=\text{COH}$  adsorbates.

At atmospheric pressure, the Cu/Ag-DA exhibits an experimental acetate selectivity of  $69 \pm 2\%$ , detected using nuclear magnetic resonance (NMR), with low ( $9 \pm 1\%$ ) hydrogen evolution reaction. This value



**Fig. 4 | CO electroreduction of Cu/Ag-DA materials at pressure.** Unless otherwise specified, experimental data reported using Cu/Ag-DA catalysts with a potential of  $-0.57$  V versus RHE in 5 M KOH in a 10-atm flow cell. **a**, Effect of CO partial pressure. **b**, Effect of applied potential. **c**, Effect of bulk Cu/(Ag+Cu) atomic ratio as measured by EDS and X-ray photoelectron spectroscopy.

**d**, Effect of host metal. **e**, Demonstration of stable operation: Cu/Ag-DA in a 10-atm membrane electrode assembly cell during 820 h of electrolysis at  $100$  mA cm $^{-2}$  current density in 2.5 M KOH. Error bars represent the standard deviation of measurements based on three independent samples.

exceeds the best previous reports<sup>5</sup> by  $1.4\times$ . We then used a pressurized flow reactor to enhance  $^{*}\text{CO}$  surface coverage (Supplementary Fig. 21), aiming to further increase FE<sub>acetate</sub>. Supplying the reactor with CO gas at 10 atm, we achieve selectivity of  $91\pm 2\%$  to acetate (Fig. 4a), and an energy efficiency of 27%. FE<sub>acetate</sub> peaks at  $-0.57$  V versus RHE and remains above 80% for a wide operating potential window (Fig. 4b and Supplementary Table 6), and within this window the energy efficiency increases to 34% (Supplementary Table 7). To check whether carbon-based products are derived from the reaction gas,  $^{13}\text{C}$ -labeling experiments with  $^1\text{H-NMR}^{33}$  and  $^{13}\text{C-NMR}^4$  were carried out: these showed that the carbon in acetate comes from  $^{13}\text{C}$  (Supplementary Figs. 22–25). The competing CORR pathways to ethylene (detected by gas chromatography; Supplementary Fig. 26) and ethanol are suppressed, leading to an increase in the acetate/(other C<sub>2+</sub>) ratio from 3.2 to 12.8 with increasing pressure. H<sub>2</sub> FE is also further suppressed at 10 atm to about 2%. Reducing CO flow to as low as 2 standard cubic centimetres per minute (SCCM; compared to 60 SCCM in other experiments) enables a single-pass utilization of CO that reaches 71%, a utilization that is accompanied by an FE<sub>acetate</sub> of 87% to acetate (Supplementary Fig. 27). Acetate FE is sensitive to KOH concentration: selectivity peaks at KOH concentrations greater than 5 M (Supplementary Fig. 28), in agreement to previous literature<sup>34</sup>.

Linking back to the host metal screening in Fig. 1, we find that catalytic trends are consistent when using the experimentally derived optimal voltage of  $-0.57$  V versus RHE in reaction energy calculations (Supplementary Fig. 2). As  $(\text{OH})\text{C}=\text{COH} \rightarrow *(\text{C}=\text{COH})$  includes an electron transfer and  $(\text{OH})\text{C}=\text{COH} \rightarrow *(\text{C}=\text{C}=\text{O})$  does not, we find the breakeven point at which the relative difference between these two pathways is zero to be at  $-0.75$  V (more negative than experimentally relevant applied potentials).

We investigated how the atomic percentage of Cu affects performance (Fig. 4c, Supplementary Table 2 and Supplementary Fig. 29). For samples with less Cu, the ratio of acetate to other C<sub>2+</sub> species remains constant, but more H<sub>2</sub> evolution is observed, a finding we attribute to an increase in undoped Ag domains. Samples with more Cu show a decrease in the acetate/(other C<sub>2+</sub>) ratio, probably related to the growth of Cu domains on the catalyst surface. Similar trends in the acetate/(other C<sub>2+</sub>) ratio were observed when we tested samples prepared through copper ion implantation onto a sputtered silver substrate (Supplementary Figs. 30 and 31). We also annealed at  $100\text{--}400$  °C and found that this produced an aggregation of nanoparticles and a lower acetate FE (Supplementary Figs. 32 and 33). CORR experiments using other Cu/M-DA catalysts (Supplementary Figs. 13–15) were optimized in a similar manner to those using Cu/Ag-DA with Cu percentage, potential and pressure as input (Supplementary Fig. 34), and the ratio of acetate to other C<sub>2+</sub> species remains the highest on Cu/Ag-DA (Fig. 4d). We also checked roles for pure Ag and carbon black: these do not show CORR activity (Supplementary Fig. 35).

The catalyst showcases an FE<sub>acetate</sub> of about 85% with <7% change for 820 h at 10 atm in a membrane electrode assembly reactor (Fig. 4e). Over this operating period, the acetate/(other C<sub>2+</sub>) ratio remains above 10 (Supplementary Figs. 36–40). In a flow cell, >88% selectivity was recovered after two sequential disassembly/reassembly cycles, a finding that suggests minimal change in catalytic activity over this operating timescale (Supplementary Fig. 41). In the flow cell, small liquid droplets are observed on the backside of the gas diffusion layer, indicating that hydrogen evolution reaction is beginning to increase as a result of flooding<sup>35</sup>.

By coupling with metrics for state-of-art CO<sub>2</sub>-to-COSOEC technology<sup>22</sup>, our 10-atm CO-to-acetate system consumes only 130 GJ of energy per

tonne of potassium acetate produced from CO<sub>2</sub> feedstock, less than half of that consumed by the best direct CO<sub>2</sub>RR system. Techno-economic analyses (see Supplementary Notes and Supplementary Figs. 42 and 43) show that operating at elevated pressure adds low dedicated capital and operating costs, and on the contrary, reduces system scale by increasing product selectivity and throughput, resulting in a net reduction in the electricity costs by 60%. The increased productivity and selectivity provides a 25% net overall cost reduction in prospective acetic acid cost estimates compared to the best previous reports<sup>5,36</sup>.

This work couples theory-guided catalyst strategy and reactor design to modulate the catalyst microenvironment. We find that combining Cu/Ag-DA catalyst materials and high-pressure CO gas leads to a preference for the monodentate \*C=C=O adsorbate and thus selectively generates acetate under high \*CO coverage, leading to an FE<sub>acetate</sub> of 91%.

## Online content

Any methods, additional references, Nature Portfolio reporting summaries, source data, extended data, supplementary information, acknowledgements, peer review information; details of author contributions and competing interests; and statements of data and code availability are available at <https://doi.org/10.1038/s41586-023-05918-8>.

1. Dinh, C. T. et al. CO<sub>2</sub> electroreduction to ethylene via hydroxide-mediated copper catalysis at an abrupt interface. *Science* **360**, 783–787 (2018).
2. Li, C. W., Ciston, J. & Kanan, M. W. Electroreduction of carbon monoxide to liquid fuel on oxide-derived nanocrystalline copper. *Nature* **508**, 504–507 (2014).
3. Zhong, M. et al. Accelerated discovery of CO<sub>2</sub> electrocatalysts using active machine learning. *Nature* **581**, 178–183 (2020).
4. Lum, Y. & Ager, J. W. Evidence for product-specific active sites on oxide-derived Cu catalysts for electrochemical CO<sub>2</sub> reduction. *Nat. Catal.* **2**, 86–93 (2019).
5. Luc, W. et al. Two-dimensional copper nanosheets for electrochemical reduction of carbon monoxide to acetate. *Nat. Catal.* **2**, 423–430 (2019).
6. Wang, X. et al. Efficient upgrading of CO to C<sub>3</sub> fuel using asymmetric C-C coupling active sites. *Nat. Commun.* **10**, 5186 (2019).
7. Jhong, H. R. M., Ma, S. & Kenis, P. J. Electrochemical conversion of CO<sub>2</sub> to useful chemicals: current status, remaining challenges, and future opportunities. *Curr. Opin. Chem. Eng.* **2**, 191–199 (2013).
8. Birdja, Y. Y. et al. Advances and challenges in understanding the electrocatalytic conversion of carbon dioxide to fuels. *Nat. Energy* **4**, 732–745 (2019).
9. Nitopi, S. et al. Progress and perspectives of electrochemical CO<sub>2</sub> reduction on copper in aqueous electrolyte. *Chem. Rev.* **119**, 7610–7672 (2019).
10. Jouny, M. et al. Formation of carbon–nitrogen bonds in carbon monoxide electrolysis. *Nat. Chem.* **11**, 846–851 (2019).
11. Kibria, M. G. et al. Electrochemical CO<sub>2</sub> reduction into chemical feedstocks: from mechanistic electrocatalysis models to system design. *Adv. Mater.* **31**, 1807166 (2019).
12. Fernández, L. *Production Capacity of Acetic Acid Worldwide in 2018 and 2023* (Statista, 2021); <https://www.statista.com/statistics/1063215/acetic-acid-production-capacity-globally/#statisticContainer>.
13. Le Berre, C., Serp, P., Kalck, P. & Torrence, G. P. in *Ullmann's Encyclopedia of Industrial Chemistry* (Ed. Ley, C.) 1–34 (Wiley-VCH, 2014).
14. Kiefer, D., Merkel, M., Lilge, L., Henkel, M. & Hausmann, R. From acetate to bio-based products: underexploited potential for industrial biotechnology. *Trends Biotechnol.* **39**, 397–411 (2021).
15. Bozzano, G. & Manenti, F. Efficient methanol synthesis: perspectives, technologies and optimization strategies. *Prog. Energy Combust. Sci.* **56**, 71–105 (2016).
16. Dimian, A. C. & Kiss, A. A. Novel energy efficient process for acetic acid production by methanol carbonylation. *Chem. Eng. Res. Des.* **159**, 1–12 (2020).
17. Kätelhön, A. et al. *Methodology cm.chemicals*. Version A (Carbon Minds, accessed 1 June 2021); [www.carbon-minds.com/cm\\_chemicals\\_methodology\\_V1.00\\_2021.pdf](http://www.carbon-minds.com/cm_chemicals_methodology_V1.00_2021.pdf).
18. Xia, C. et al. Continuous production of pure liquid fuel solutions via electrocatalytic CO<sub>2</sub> reduction using solid-electrolyte devices. *Nat. Energy* **4**, 776–785 (2019).
19. Ripatti, D. S., Veltman, T. R. & Kanan, M. W. Carbon monoxide gas diffusion electrolysis that produces concentrated C<sub>2</sub> products with high single-pass conversion. *Joule* **3**, 240–256 (2019).
20. Zhu, P. et al. Direct and continuous generation of pure acetic acid solutions via electrocatalytic carbon monoxide reduction. *Proc. Natl Acad. Sci. USA* **118**, e2010868118 (2021).
21. Zang, D. et al. Interface engineering of Mo<sub>3</sub>/Cu heterostructures toward highly selective electrochemical reduction of carbon dioxide into acetate. *Appl. Catal. B* **281**, 119426 (2021).
22. Li, Y. et al. A novel fuel electrode enabling direct CO<sub>2</sub> electrolysis with excellent and stable cell performance. *J. Mater. Chem. A* **5**, 20833–20842 (2017).
23. Hauch, A. et al. Recent advances in solid oxide cell technology for electrolysis. *Science* **370**, eaba6118 (2020).
24. Ozden, A. et al. Cascade CO<sub>2</sub> electroreduction enables efficient carbonate-free production of ethylene. *Joule* **5**, 706–719 (2021).
25. Jouny, M., Hutchings, G. S. & Jiao, F. Carbon monoxide electroreduction as an emerging platform for carbon utilization. *Nat. Catal.* **2**, 1062–1070 (2019).
26. Hori, Y., Murata, A. & Takahashi, R. Formation of hydrocarbons in the electrochemical reduction of carbon dioxide at a copper electrode in aqueous solution. *J. Chem. Soc. Faraday Trans.* **185**, 2309–2326 (1989).
27. Zhan, C. et al. Revealing the CO coverage-driven C-C coupling mechanism for electrochemical CO<sub>2</sub> reduction on Cu<sub>2</sub>O nanocubes *via* operando Raman spectroscopy. *ACS Catal.* **11**, 7694–7701 (2021).
28. Deshpande, S., Maxson, T. & Greeley, J. Graph theory approach to determine configurations of multidentate and high coverage adsorbates for heterogeneous catalysis. *npj Comput. Mater.* **6**, 79 (2020).
29. Kim, D., Resasco, J., Yu, Y., Asiri, A. M. & Yang, P. Synergistic geometric and electronic effects for electrochemical reduction of carbon dioxide using gold–copper bimetallic nanoparticles. *Nat. Commun.* **5**, 4948 (2014).
30. Guo, H., Chen, Y., Ping, H., Wang, L. & Peng, D. L. One-pot synthesis of hexagonal and triangular nickel–copper alloy nanoplates and their magnetic and catalytic properties. *J. Mater. Chem.* **22**, 8336–8344 (2012).
31. Li, J. et al. Copper adparticle enabled selective electrosynthesis of n-propanol. *Nat. Commun.* **9**, 4614 (2018).
32. Zhang, X. et al. Molecular engineering of dispersed nickel phthalocyanines on carbon nanotubes for selective CO<sub>2</sub> reduction. *Nat. Energy* **5**, 684–692 (2020).
33. Karapinar, D. et al. Electrocatalysis of CO<sub>2</sub> on single-site copper–nitrogen-doped carbon material: selective formation of ethanol and reversible restructuration of the metal sites. *Angew. Chem. Int. Ed.* **58**, 15098–15103 (2019).
34. Ma, M. et al. Local reaction environment for selective electroreduction of carbon monoxide. *Energy Environ. Sci.* **15**, 2470–2478 (2022).
35. Ma, S. et al. One-step electrosynthesis of ethylene and ethanol from CO<sub>2</sub> in an alkaline electrolyzer. *J. Power Sources* **301**, 219–228 (2016).
36. Ji, Y. et al. Selective CO-to-acetate electroreduction via intermediate adsorption tuning on ordered Cu–Pd sites. *Nat. Catal.* **5**, 251–258 (2022).

**Publisher's note** Springer Nature remains neutral with regard to jurisdictional claims in published maps and institutional affiliations.

Springer Nature or its licensor (e.g. a society or other partner) holds exclusive rights to this article under a publishing agreement with the author(s) or other rightsholder(s); author self-archiving of the accepted manuscript version of this article is solely governed by the terms of such publishing agreement and applicable law.

© The Author(s), under exclusive licence to Springer Nature Limited 2023

# Article

## Methods

### Computational methods

The models for the CO-to-acetate electrocatalyst design (Fig. 1) were built using the atomic simulation environment (ASE) python package<sup>37</sup>. A  $3 \times 3 \times 4$  slab of the (111) facet was used for all calculations. The bottom two layers of the slab were fixed. For the Cu<sub>1</sub>Ag<sub>35</sub> model as an example, one surface atom of an Ag surface was substituted for a Cu atom and then relaxed. The appropriate adsorbate and charged water layer were added to the relaxed surface. For efficiency, the structures were first relaxed without dipole corrections, and then dipole corrections were applied afterwards. Spin polarization was used in the Cu<sub>1</sub>Ni<sub>35</sub> models. The charged water layer is defined as a monolayer of six water molecules above the surface, in which one of the six water molecules is protonated (H<sub>3</sub>O<sup>+</sup>). This structure is used to account for field and solvation effects<sup>38</sup>. The water layer structure was previously determined by ab initio molecular dynamics and was free to relax during density functional theory (DFT) calculations<sup>6</sup>.

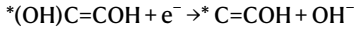
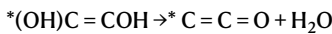
Vienna Ab initio Simulation Package (v5.4.4) was used for DFT calculations. The generalized gradient approximation and the Perdew–Burke–Ernzerhof exchange-correlation functional were used. Electron–ion interactions were addressed with the projector augmented wave method<sup>39–45</sup>. Previous works in CO<sub>2</sub> electrocatalysis have used a similar set of calculation parameters<sup>46–48</sup>.

Example INCAR, KPOINTS and submission files are provided, along with the relaxed structures of all models used in calculations. DFT parameters include a plane-wave basis set energy cutoff of 450 eV, a force convergence of 0.01 eV Å<sup>-1</sup>, an energy convergence of 10<sup>-5</sup> eV, a  $3 \times 3 \times 1$  Monkhorst *k*-point grid, and a 15-Å vacuum gap above the slab.

The Gibb's free energy was calculated by the equation:

$$\Delta G = \Delta E_{\text{elec}} + \Delta E_{\text{ZPE}} + \int_0^{298} \Delta C_p dT - T \Delta S$$

in which  $E_{\text{elec}}$  is the electronic energy from DFT calculations,  $E_{\text{ZPE}}$  is the zero-point energy,  $C_p$  is the heat capacity, and  $S$  is entropy. Zero-point energy, heat capacity and entropy are calculated through vibrational analysis.



The first equation represents the pathway towards acetate and the second equation represents the pathway towards other C<sub>2+</sub> species such as ethylene and ethanol.

In Fig. 1b, ASE was used to generate a list of all possible adsorption sites on the surface referenced to one carbon in the (OH)C=COH, C=C=O and C=COH adsorbates. Structure energies were calculated for at least ten adsorption positions for each adsorbate on each of the five surfaces. The lowest energy configuration was used following a check that the integrity of the adsorbate was maintained. For example, if an adsorbate dissociated into two adsorbates, was protonated or changed from bidentate to monodentate, the configuration was not used in further calculations.

In Fig. 1c, two \*CO species were modelled explicitly in the C–C coupling calculation to ensure consistent C coverage on the surface in initial and final states.

In calculations with multiple adsorbates (Fig. 1d), ASE was used to generate combinations of adsorbate sites with a 3-Å radius to prevent overlap (including on top, bridge and hollow sites). Adsorbates were placed at 10–20 randomly selected configurations. The lowest energy configuration (most stable) was used throughout.

### XANES calculations

**WIEN 2k.** The theoretical XANESs of Cu–Ag compounds were calculated using DFT<sup>49,50</sup> in WIEN 2k<sup>51</sup>. The program uses the linearized augmented plane-wave method. We have used the generalized gradient approximation<sup>52</sup> to calculate self-consistently the ground-state energies for these compounds. The program starts with the crystal structures of a model compound, and calculates the energy levels by iterations until the energies have been reached within 0.0001 Ry. The XANES spectra are then obtained by the transitions between these energy levels following the selection rule. Owing to the small amount of Cu in our samples, Cu atoms do not form a crystal with Ag, but form Cu atomic clusters on the surface of Ag.

**FEFF9 theory.** The theoretical XANES spectra have also been calculated by FEFF9 theory<sup>53</sup>. FEFF9 is based on the real-space multiple scattering theory. It starts with a cluster based on the input file, atom.inp. The input files, atom.inp and feff.inp, are derived by the program Artemis<sup>54</sup>, starting with the face-centred cubic (fcc) Ag cif file and having a small number of Ag substituted by Cu atoms.

### Theoretical prediction of Raman peaks

The vibrational frequencies of adsorbed species were numerically calculated using the Vienna ab initio simulation package using the harmonic approximation, which uses a fixed substrate. The corresponding second derivatives of the potential energy matrix with respect to atomic displacements were calculated using two finite-difference steps (NFREE = 2) and atomic movements of 0.015 Å (POTIM) in each of the three Cartesian directions, and the resulting dynamical matrix was diagonalized. Other parameters are the same as in the calculations above.

### Materials synthesis

The precursor chemicals used in this work were silver nitrate (AgNO<sub>3</sub>, 99.5%, Aldrich), oleylamine (C<sub>18</sub>H<sub>37</sub>N, 80–90%, Aldrich), copper (II) chloride dihydrate (CuCl<sub>2</sub>·H<sub>2</sub>O, 99.5%, Loba Chemie), gold chloride solution (HAuCl<sub>4</sub>, 23.5–23.8%, Aldrich), nickel acetylacetone (NiC<sub>10</sub>H<sub>14</sub>O<sub>4</sub>, 95%, Aldrich), 1-octadecene (C<sub>18</sub>H<sub>36</sub>, >90%, Aldrich), hexane (C<sub>6</sub>H<sub>14</sub>, 98.7%, BioslabChile) and isopropanol (C<sub>3</sub>H<sub>8</sub>O, Loba Chemie). All reagents were used as received without any purification.

Cu-in-M dilute alloy (Cu/M-DA) (M = Ag, Au or NiO) catalysts were synthesized through the co-reduction of metal precursors. In all experiments, CuCl<sub>2</sub>·H<sub>2</sub>O was used as the copper source because the coexistence of Cl<sup>-</sup> and Cu<sup>2+</sup> helps to tune the nucleation energy of Cu. In this way, the nucleation rate of Cu can be much lower than that of M (Ag, Au or NiO)<sup>29,30,55</sup>.

For the Cu/Ag-DA catalysts, 0.8 mmol AgNO<sub>3</sub>, 0.4 mmol CuCl<sub>2</sub>·H<sub>2</sub>O and 5 ml oleylamine were added into a 100-ml beaker, and then the mixtures were stirred magnetically at 80 °C for 20 min. Subsequently, the solution was transferred into a 100-ml Teflon-lined autoclave and heated to 175 °C for 10 h. After the mixture solution was naturally cooled down to room temperature, the Cu/Ag-DA nanoparticles were collected by centrifugation at 8,000 r.p.m. The collected products were re-dispersed in hexane and washed with isopropanol for further characterization.

The synthetic procedure for Cu/Ni-DA catalysts was identical to the synthesis of Cu/Ag-DA catalysts, except for the use of different precursor (NiC<sub>10</sub>H<sub>14</sub>O<sub>4</sub>) and an increased reaction temperature of 200 °C (guaranteeing the formation of Ni).

Cu/Au-DA catalysts were prepared with methods modified from a previous report<sup>29</sup>. Volumes of 20 ml 1-octadecene and 2 ml oleylamine were mixed and heated to 100 °C for 30 min under nitrogen atmosphere. After the solution cooled to room temperature, 0.3 mmol HAuCl<sub>4</sub> and 0.15 mmol CuCl<sub>2</sub>·H<sub>2</sub>O were added into the mixture and stirred magnetically at 80 °C for 20 min. Afterwards, it was further heated to 280 °C for

20 min. After the reaction, 20 ml isopropanol was added to precipitate the nanoparticles, and the product was collected by centrifugation at 8,000 r.p.m. The collected products were re-dispersed in hexane and washed with isopropanol for further characterization.

As a post-treatment of Cu/Ag-DA nanoparticles and to avoid the oxidation of Ag during the annealing process, the prepared Cu/Ag-DA gas diffusion electrodes (GDEs) were heated to annealing temperature ( $T = 100\text{--}400^\circ\text{C}$ ) for 30 min under a nitrogen atmosphere with a  $3\text{ }^\circ\text{C min}^{-1}$  heating rate.

### Preparation of GDEs

The collected Cu/Ag-DA nanoparticles were dispersed in 3 ml methanol and 30  $\mu\text{l}$  Nafion (5 wt%, Sigma-Aldrich) under ultrasonication for 30 min. The solution was spray-coated onto a Freudenberg gas diffusion layer (H14C9) with a catalyst loading of  $\approx 0.2\text{ mg}\cdot\text{cm}^{-2}$ .

### CORR in a pressurized flow cell

CORR experiments were carried out in a homemade pressurized flow cell (Supplementary Fig. 21) consisting of a catalyst-deposited GDE as the working electrode, an anion exchange membrane (Fumasep FAA-PK-130) and nickel foam (1.6 mm thickness, MTI Corporation) as the anode. The cell was powered by an electrochemical workstation (Autolab PGSTAT302N) and referenced to an Ag/AgCl electrode (saturated KCl as filling solution). An electrolyte of 5 M KOH with a volume of 20 ml was used in all experiments. The flow rates of CO gas and electrolyte were set to 60 SCCM and  $20\text{ ml min}^{-1}$ , respectively.

A cell resistance ( $R_{\text{cell}}$ ) of  $0.85\ \Omega$  was measured by the electrochemical workstation,  $iR$  correction was carried out using the equation:

$$(E_{\text{Ag/AgCl}})_{iR} = E_{\text{Ag/AgCl}} - 0.85 \times i \times R_{\text{cell}}$$

in which  $E_{\text{Ag/AgCl}}$  is the applied potential before  $iR$  compensation and  $i$  is the total current.

Applied cathode potentials were converted to the RHE scale using:

$$E_{\text{RHE}} = (E_{\text{Ag/AgCl}})_{iR} + 0.195\text{ V} + 0.0591 \times \text{pH}$$

The full-cell energy efficiency for acetate production is calculated as follows<sup>56</sup>:

$$\text{EE}_{\text{acetate,full-cell}} = \frac{(1.23 - E_{\text{acetate}}) \times \text{FE}_{\text{acetate}}}{E_{\text{cell}}}$$

in which  $E_{\text{cell}}$  is the applied cell voltage,  $\text{FE}_{\text{acetate}}$  is the measured FE of acetate, and  $E_{\text{acetate}}$  is the thermodynamic potential of CO electroreduction to acetate (that is,  $0.32\text{ V}$ )<sup>9</sup>.

Gas products ( $\text{H}_2$ ,  $\text{CH}_4$  and  $\text{C}_2\text{H}_4$ ) were analysed using a gas chromatograph (Shimadzu GC-2014) coupled with a thermal conductivity detector (for  $\text{H}_2$ ) and two flame ionization detectors (for  $\text{CH}_4$  and  $\text{C}_2\text{H}_4$ , respectively). The liquid products in the catholyte were quantified with  $^1\text{H}$  spectroscopy on a Bruker 600-MHz spectrometer, and dimethylsulfoxide was used as an internal standard. The samples were taken from the catholyte every 10 min, and 50  $\mu\text{l}$  of the sample was mixed with 450  $\mu\text{l}$   $\text{D}_2\text{O}$  and 100  $\mu\text{l}$  dimethylsulfoxide (about 50 ppm) to measure the liquid products. For liquid product detection in  $^{13}\text{CORR}$  experiments, both  $^1\text{H}$  spectroscopy and  $^{13}\text{C}$  spectroscopy were used; corresponding detection methods can be found in refs. 4,33.

### CORR in a pressurized membrane electrode assembly

CORR stability experiments were carried out in a homemade pressurized membrane electrode assembly cell (Supplementary Figs. 36 and 39) consisting of a catalyst-deposited GDE as the working electrode, an anion exchange membrane (Fumasep FAA-PK-130) and nickel foam (1.6 mm thickness, MTI Corporation) as the anode. Anode and cathode flow-field plates had a geometric area of  $1\text{ cm}^2$ . The cell was powered by

an electrochemical workstation (Autolab PGSTAT302N); the current density was set to  $100\text{ mA cm}^{-2}$ . An electrolyte of 2.5 M KOH was used in the experiments. The flow rates of CO gas and electrolyte were set to 6.8 SCCM and  $0.5\text{ ml min}^{-1}$ , respectively. Gas and liquid products were detected using the same methods as above.

### Materials characterization

Structural characterization of the as-synthesized catalysts was carried out using X-ray diffraction (MiniFlex600) with Cu-K $\alpha$  radiation. SEM images were taken using a Quanta FEG 250 microscope. TEM, high-resolution TEM and EDS mapping images were recorded by a Quanta FEG 250. The surface composition was determined by X-ray photoelectron spectroscopy (model 5600, Perkin-Elmer) using a monochromatic aluminium X-ray source. Atomic-resolution HAADF images and the electron energy-loss spectrum (EELS) analysis were carried out on the JEOL ARM 200 CF microscope at 200 kV. This microscope was equipped with a cold field-emission gun, a CEOS probe corrector and a Gatan Quantum image filtering system. The Gatan image filtering system was updated with a K2-IS direct detector. The spatial resolution in scanning TEM mode is less than  $0.8\text{ \AA}$ . The convergence semi-angle for HAADF imaging and spectrum imaging is 30 mrad. The collection semi-angle for HAADF imaging and spectrum imaging is in the range of 90–370 mrad and 0–84 mrad. The used energy dispersion for spectrum imaging is 0.25 eV per pixel and the energy resolution is around 1.5 eV determined by using the full-width at half-maximum method. The background of EELS analysis was subtracted using a power-law fitting method. To improve the signal–noise ratio of the atomic-resolution EELS mapping, we used the principal component analysis method during the post processing.

### Calculation of turnover frequency and turnover number

We assume that all Cu atoms participate in the catalytic reaction, owing to the low (1%) overall concentration of Cu and challenges in measuring the surface fraction of such a low Cu concentration. This assumption gives an under-estimation to the turnover frequency (TOF). The following formula was used to estimate the TOF<sup>57</sup>:

$$\text{TOF (s}^{-1}\text{)} = \frac{j_{\text{AcO}}/(NF)}{m_{\text{cat}}\omega/M_{\text{Ag}}}$$

in which  $j_{\text{AcO}}$ ,  $N$ ,  $F$ ,  $m_{\text{cat}}$ ,  $\omega$  and  $M_{\text{Ag}}$  denote the partial current density of acetate (taken from the highest FE case instead of the highest current case), the number of electrons transferred (4) in the CO-to-acetate conversion, the Faradaic constant, the catalyst mass loading, the Cu atomic fraction in the Cu/Ag-DA, and the atomic mass of Ag (major content of the Cu/Ag-DA), respectively. The resultant TOF is  $31.3\text{ s}^{-1}$ .

The same assumption, all Cu participating in the reaction, is made for the estimation of the turnover number (TON). It is the total amount of acetate produced normalized by the amount of the Cu sites<sup>58</sup>:

$$\text{TON} = \frac{j_{\text{AcO}}/(NF) \times t}{m_{\text{cat}}\omega/M_{\text{Ag}}}$$

in which  $t$  is the duration of electrolyser operation. We estimate a TON of  $1.24 \times 10^7$  using performance data from the 10-atm membrane electrode assembly experiments.

### In situ Raman spectroscopy

In situ Raman spectroscopy was carried out using a Horiba LabRAM HR Evolution microscope. The Raman spectra were acquired with a He/Ne laser of  $\lambda = 532\text{ nm}$  and  $4.9\text{ mW}$ . A series of neutral density filters were used to reduce the incident energy to  $<0.2\text{ mW}$  in all experiments to minimize sample damage. The scattered Raman light was collected using a  $50\times$  Leica lens (numerical aperture of 0.5) and the wavenumber calibration was carried out using a Si wafer. Freshly prepared 5 M KOH

# Article

solution was used as the electrolyte. The electrolyte was pumped into a custom-made three-electrode electrochemical cell at a rate of  $5 \text{ ml min}^{-1}$  using a peristaltic pump. The reference and counter electrodes used were a single-junction Ag/AgCl electrode and a graphite rod. The working electrode consisted of Cu/Ag-DA samples, and the area exposed to the electrolyte was about  $0.8 \text{ cm}^2$ . Before the *in situ* experiments, new silicone gaskets were cut and rinsed with copious amounts of isopropanol and deionized water, and they were stored in deionized water overnight. On the day of the experiment, the storage deionized water was replaced with fresh deionized water from the Millipore machine. Potential-dependent *in situ* Raman spectroscopy was carried out using a 116-s acquisition time with an accumulation time of 6 s.

## Data availability

The datasets supporting the findings of this article are included in the article and its Supplementary Information.

37. Hjorth Larsen, A. et al. The atomic simulation environment - a Python library for working with atoms. *J. Phys. Condens. Matter* **29**, 273002 (2017).
38. Montoya, J. H., Shi, C., Chan, K. & Nørskov, J. K. Theoretical insights into a CO dimerization mechanism in  $\text{CO}_2$  electroreduction. *J. Phys. Chem. Lett.* **6**, 2032–2037 (2015).
39. Kresse, G. & Hafner, J. Ab initio molecular-dynamics simulation of the liquid-metalamorphous-semiconductor transition in germanium. *Phys. Rev. B* **49**, 14251–14269 (1994).
40. Kresse, G. & Furthmüller, J. Efficient iterative schemes for ab initio total-energy calculations using a plane-wave basis set. *Phys. Rev. B* **54**, 1169–1186 (1996).
41. Kresse, G. & Furthmüller, J. Efficiency of ab-initio total energy calculations for metals and semiconductors using a plane-wave basis set. *Comput. Mater. Sci.* **6**, 15–50 (1996).
42. Kresse, G. & Hafner, J. Ab initio molecular dynamics for liquid metals. *Phys. Rev. B* **47**, 558–561 (1993).
43. Perdew, J. P., Burke, K. & Ernzerhof, M. Generalized gradient approximation made simple. *Phys. Rev. Lett.* **77**, 3865–3868 (1996).
44. Blöchl, P. E. Projector augmented-wave method. *Phys. Rev. B* **50**, 17953–17979 (1994).
45. Kresse, G. & Joubert, D. From ultrasoft pseudopotentials to the projector augmented-wave method. *Phys. Rev. B* **59**, 1758–1775 (1999).
46. Wang, X. et al. Gold-in-copper at low \*CO coverage enables efficient electromethanation of  $\text{CO}_2$ . *Nat. Commun.* **12**, 3387 (2021).
47. Wang, X. et al. Efficient methane electrosynthesis enabled by tuning local  $\text{CO}_2$  availability. *J. Am. Chem. Soc.* **142**, 3525–3531 (2020).
48. Wang, X. et al. Efficient electrosynthesis of n-propanol from carbon monoxide using a Ag-Ru-Cu catalyst. *Nat. Energy* **7**, 170–176 (2022).
49. Hohenberg, P. & Kohn, W. Inhomogeneous electron gas. *Phys. Rev.* **136**, B864–B871 (1964).
50. Kohn, W. & Sham, L. J. Self-consistent equations including exchange and correlation effects. *Phys. Rev.* **140**, A1133–A1138 (1965).
51. Blaha, P., Schwarz, K., Sorantin, P. & Trickey, S. B. Full-potential, linearized augmented plane wave programs for crystalline systems. *Comput. Phys. Commun.* **59**, 399–415 (1990).
52. Perdew, J. P. & Wang, Y. Accurate and simple analytic representation of the electron-gas correlation energy. *Phys. Rev. B* **45**, 13244–13249 (1992).
53. Rehr, J. J. & Albers, R. C. Theoretical approaches to x-ray absorption fine structure. *Rev. Mod. Phys.* **72**, 621–654 (2000).
54. Ravel, B. & Newville, M. ATHENA, ARTEMIS, HEPHAESTUS: data analysis for X-ray absorption spectroscopy using IFEFFIT. *J. Synchrotron Radiat.* **12**, 537–541 (2005).
55. Freire, R. M. et al. Natural arrangement of AgCu bimetallic nanostructures through oleylamine reduction. *Inorg. Chem. Front.* **7**, 4902–4912 (2020).
56. Li, F. et al. Molecular tuning of  $\text{CO}_2$ -to-ethylene conversion. *Nature* **577**, 509–513 (2020).
57. Zhang, B. et al. Manganese acting as a high-performance heterogeneous electrocatalyst in carbon dioxide reduction. *Nat. Commun.* **10**, 2980 (2019).
58. Ogihara, H., Maezuru, T., Ogishima, Y. & Yamanaka, I. Electrocatalytic activity of Co-4,4'dimethyl-2,2'-bipyridine supported on Ketjenblack for reduction of  $\text{CO}_2$  to CO using PEM reactor. *Electrocatalysis* **9**, 220–225 (2018).

**Acknowledgements** Y.P. acknowledges financial support from the National Key R&D Program of China (grant number 2022YFC2106000), the National Natural Science Foundation of China (grant number 11874164) and the Innovation Fund of Wuhan National Laboratory for Optoelectronics. J.J. acknowledges financial support from the National Natural Science Foundation of China (grant number 52006085) and the China Postdoctoral Science Foundation (grant numbers 2019TQ0104 and 2020M672343). L.M. acknowledges financial support from the National Natural Science Foundation of China (grant numbers 52127816 and 51832004) and the National Key Research and Development Program of China (grant number 2020YFA0715000). J.L. acknowledges financial support from the National Natural Science Foundation of China (grant number BE3250011), the National Key Research and Development Program of China (grant number 2022YFA1505100) and Shanghai Jiao Tong University (grant number WH220432516). E.H.S. acknowledges financial support from the Natural Sciences and Engineering Research Council of Canada (NSERC) Discovery programme (grant number RGPIN-2017-06477) and the Ontario Research Fund (grant number ORF-RE08-034). J.W. acknowledges support from the NSERC Postgraduate Scholarship – Doctoral (PGS-D). Z.W. acknowledges financial support from the Marsden Fund Council for Government funding (grant number 21-UOA-237) and the Catalyst: Seeding General Grant (grant number 22-UOA-031-CGS), managed by the Royal Society Te Apārangi. C.W. acknowledges financial support from the National Natural Science Foundation of China (grant numbers 51972129 and 52272202). Figure 1a was created with BioRender.com. The DFT computations in Fig. 1 exploring reaction pathways were carried out on the Niagara supercomputer at the SciNet HPC Consortium. SciNet is funded by the Canada Foundation for Innovation, the Government of Ontario, the Ontario Research Fund Research Excellence Program and the University of Toronto. This work made use of the EPIC facility of Northwestern University's NUANCE Center, which has received support from the SHyNE Resource (grant number NSF ECCS-2025633), the IIN and Northwestern's MRSEC programme (grant number NSF DMR-1720139). Part of the research described in this paper was carried out at the Canadian Light Source, a national research facility of the University of Saskatchewan, which is supported by the Canada Foundation for Innovation, NSERC, the National Research Council, the Canadian Institutes of Health Research, the Government of Saskatchewan and the University of Saskatchewan. We thank beamline BL14W1 (X-ray absorption fine structure) at SSRF for providing the beamtime, and also acknowledge the support of the Analytical and Testing Center of Huazhong University of Science and Technology for X-ray diffraction, X-ray photoelectron spectroscopy, inductively coupled plasma optical emission spectroscopy, SEM and TEM measurements.

**Author contributions** Y.P., E.H.S., D.S., Z.W. and L.M. supervised the project. J.J. designed the high-pressure electrocatalytic system and carried out electrochemical experiments. Q.M. completed catalyst synthesis and most of its characterization (TEM, X-ray photoelectron spectroscopy, X-ray diffraction and inductively coupled plasma). J.W. carried out DFT calculations. J.L., P.P., J.W., Y.H., M.S., Q.X., J.M., Y.W., Y.X., Y.P. and Z.J. carried out XAS measurements, and J.L. analysed the XAS data. L.M., R.L., P.Q., Y.P., Z.C., W.Z. and K.Y. carried out Raman characterization, and J.W. analysed the Raman data. R.L. and Y.M. conducted vibrational frequency calculations. J.J., G.S. and Q.M. carried out membrane electrode assembly stability tests. Y.X. and A.O. contributed preliminary stability measurements. J.S. and X.J. carried out NMR measurements. Q.M., Y.L., D.W. and P.Q. carried out SEM measurements. X.H. and V.P.D. carried out the HAADF scanning TEM measurements. Y.-M.Y. and T.-K.S. completed the XANES fitting. J.W. conducted the techno-economic assessment. P.O., X.W., Z.W., C.W., B.Y.X. and D.S. contributed to data analysis. J.J., J.W., Q.M., J.L., Y.P. and E.H.S. co-wrote the manuscript. All authors discussed the results and assisted during manuscript preparation.

**Competing interests** The authors declare no competing interests.

### Additional information

**Supplementary information** The online version contains supplementary material available at <https://doi.org/10.1038/s41586-023-05918-8>.

**Correspondence and requests for materials** should be addressed to Liqiang Mai, Edward H. Sargent or Yuanjie Pang.

**Peer review information** *Nature* thanks Feng Jiao, Yongge Wei and the other, anonymous, reviewer(s) for their contribution to the peer review of this work.

**Reprints and permissions information** is available at <http://www.nature.com/reprints>.